

lion years (MSWD = 112) with an initial $^{187}\text{Os}/^{188}\text{Os}$ value of 1.6 ± 1.5 (Fig. 1D). The VCR pyrites have low Os concentrations (9 to 20 parts per trillion); therefore, their Os isotopic compositions are more prone to being altered through interactions with later Os-bearing fluids than VR gold and pyrite with higher Os concentrations. The scattered distribution of the VCR pyrite Re-Os data likely has no age relevance, but rather reflects postdepositional disturbance or averaging of different authigenic generations of VCR pyrite.

VR gold and pyrite have much larger Os concentrations than the VCR pyrite (Table 1), suggesting a deposition mechanism different from the epigenetic precipitation of the VCR pyrite. The higher Os concentrations of the VR gold and pyrite would also imply that their geochronologic information is more unlikely to have been disturbed by later precipitation or mobilization of Os by hydrothermal fluids.

A mantle or mantle-derived mafic/ultramafic rock source for the WSG gold and rounded pyrite is indicated by initial $^{187}\text{Os}/^{188}\text{Os}$ values of 0.109 (VR-Au isochron) and 0.108 (VR-Au and Pyr isochron), corresponding to the estimated Os isotopic composition of the mantle at about 3.0 Ga (6). Supporting evidence for a mantle origin of WSG gold is provided by the higher Os concentration of the WSG gold relative to the VCR pyrite, the gold and pyrite from other hydrothermal gold deposits, and the younger (~2.2 Ga) Moeda Formation paleoplacer deposit (Fig. 2) (21, 22). Minerals from these younger deposits have low Os concentrations and high Re/Os ratios similar to those of evolved crustal rocks. The WSG gold, and to a lesser extent rounded pyrites, have high Os concentrations and low Re/Os ratios more similar to those of mantle rocks and primary S-rich komatiites (Fig. 2).

The age of the VR gold and pyrite may reflect the age of the mineralization event in the source rock(s) they were derived from, whereas the initial $^{187}\text{Os}/^{188}\text{Os}$ value constrains the source area of that rock. When plotted together, the VR gold and pyrites yield a precise age of 3.03 ± 0.02 Ga with a homogeneous, unradiogenic (mantle-like) initial value and may indicate that both gold and pyrite mineralization are cogenetic. This age is similar to the 3.08-Ga peak in WSG detrital zircon ages (2). Zircons of this age reflect an increasing evolved granitic crustal input, as well as an increase in basaltic/greenstone components delivered to the WSG sediments. These components are possibly derived from erosion of 3.08-Ga basalts of the Dominion Group and the 3.07- to 2.97-Ga Murchison greenstone belt (2, 23). Although the Dominion Group is not a likely source of large amounts of gold, contemporaneous subaqueous expressions of mafic magmatism in the form of gold-rich sulfide-facies exhalites may have been a potential source (24). The Murchison greenstone belt and possible equivalents along the

Thabazimbi-Murchison lineament are candidates for the source of gold to the WSG (23). The initial $^{187}\text{Os}/^{188}\text{Os}$ value of WSG gold (0.109) is consistent with gold emplacement into the crust by mantle-derived basaltic/greenstone magmatism at ~3.0 Ga.

References and Notes

1. H. E. Frimmel, W. E. L. Minter, *Soc. Econ. Geol. Spec. Publ.* **9**, 17 (2002).
2. L. J. Robb, F. M. Meyer, *Ore Geol. Rev.* **10**, 67 (1995).
3. C. C. Rundle, N. J. Snelling, *Philos. Trans. R. Soc. London Ser. A* **286**, 567 (1977).
4. R. Saager, *U.S. Geol. Surv. Prof. Pap.* **1161-L**, 1 (1981).
5. S. R. Hart, E. D. Kinloch, *Econ. Geol.* **84**, 1651 (1989).
6. J. Kirk, J. Ruiz, J. Chesley, S. Titley, J. Walshe, *Geochim. Cosmochim. Acta* **65**, 2149 (2001).
7. R. E. Zartman, H. E. Frimmel, *Mineral. Petrol.* **66**, 171 (1999).
8. H. E. Frimmel, *J. Geol.* **105**, 601 (1997).
9. G. L. England et al., *Terra Nova* **13**, 1 (2001).
10. M. P. Coward, R. M. Spencer, C. E. Spencer, in *Early Precambrian Processes*, M. P. Coward, A. C. Reis, Eds. (Geological Society of London, Spec. Publ. 95, 1995), p. 243.
11. W. E. L. Minter, *Min. Eng.* **42**, 195 (1990).
12. M. Poujol, L. J. Robb, J. P. Respaut, *Precambrian Res.* **95**, 167 (1999).
13. E. T. Mellor, *Trans. Inst. Min. Metall.* **25**, 226 (1916).
14. D. K. Hallbauer, T. Utter, *Miner. Deposita* **12**, 296 (1977).
15. L. C. Graton, *Econ. Geol.* **25** (suppl. 3), 1 (1930).
16. G. N. Phillips, D. M. Law, *Ore Geol. Rev.* **9**, 1 (1994).
17. A. C. Barnicoat et al., *Nature* **386**, 820 (1997).

18. S. B. Shirey, R. J. Walker, *Annu. Rev. Earth Planet. Sci.* **26**, 423 (1998).
19. W. E. L. Minter, *Econ. Geol.* **94**, 665 (1999).
20. Materials and methods are available as supporting material on Science Online.
21. J. Kirk, unpublished data.
22. W. E. L. Minter, F. E. Renger, A. Siegers, *Econ. Geol.* **85**, 943 (1990).
23. M. Poujol, L. J. Robb, J. P. Respaut, C. R. Anhaeusser, *Econ. Geol.* **91**, 1455 (1996).
24. R. W. Hutchinson, R. P. Viljoen, *S. Afr. J. Geol.* **91**, 157 (1988).
25. K. R. Ludwig, *U.S. Geol. Surv. Open File Rep.* 91-445 (1991).
26. D. D. Lambert, J. G. Foster, L. R. Frick, *Econ. Geol.* **93**, 121 (1998).
27. B. K. Esser, K. K. Turekian, *Geochim. Cosmochim. Acta* **57**, 3093 (1993).
28. B. Peucker-Ehrenbrink, B. Jahn, *G³* **2**, paper no. GC000172 (2001).
29. We thank M. Baker for managing the isotopic laboratory and N. Fox (AngloGold) for help with providing Vaal Reef samples. We appreciate thoughtful reviews by F. Barra, R. Mathur, Z. Naiman, and three anonymous reviewers that improved this manuscript. Analytical work was funded by the National Science Foundation (grants EAR 9708361 and EAR 9628150). Re-Os analyses were performed at the Keck laboratory, University of Arizona.

Supporting Online Material

www.sciencemag.org/cgi/content/full/297/5588/1856/DC1
 Material and Methods
 Fig. S1

19 June 2002; accepted 31 July 2002

Deformation on Nearby Faults Induced by the 1999 Hector Mine Earthquake

Yuri Fialko,^{1*} David Sandwell,¹ Duncan Agnew,¹ Mark Simons,² Peter Shearer,¹ Bernard Minster¹

Interferometric Synthetic Aperture Radar observations of surface deformation due to the 1999 Hector Mine earthquake reveal motion on several nearby faults of the eastern California shear zone. We document both vertical and horizontal displacements of several millimeters to several centimeters across kilometer-wide zones centered on pre-existing faults. Portions of some faults experienced retrograde (that is, opposite to their long-term geologic slip) motion during or shortly after the earthquake. The observed deformation likely represents elastic response of compliant fault zones to the permanent co-seismic stress changes. The induced fault displacements imply decreases in the effective shear modulus within the kilometer-wide fault zones, indicating that the latter are mechanically distinct from the ambient crustal rocks.

Stress and strain transfer within seismogenic fault systems is a well-documented yet poorly understood phenomenon. It is known that earthquakes can activate nearby (or, sometimes, dis-

tant) faults, causing variations in local seismicity rates or triggering aseismic fault slip (1-3). Detailed studies using Interferometric Synthetic Aperture Radar (InSAR) data from several large strike-slip earthquakes, including the 1992 M_w 7.3 Landers earthquake (where M_w is the moment magnitude) (4), the 1999 M_w 7.6 Izmit earthquake (5), and the 1999 M_w 7.1 Hector Mine earthquake (6, 7), revealed ubiquitous displacements on pre-existing faults in the vicinity of the mainshock rupture. In some instances, the sense of fault motion has been

¹Institute of Geophysics and Planetary Physics, Scripps Institution of Oceanography, University of California San Diego, La Jolla, CA 92093, USA. ²Seismological Laboratory, Division of Geological and Planetary Sciences, California Institute of Technology, Pasadena, CA 91125 USA.

*To whom correspondence should be addressed. E-mail: fialko@radar.ucsd.edu.

REPORTS

inferred to be opposite to the long-term fault slip and regional stress orientation (5, 6, 8). If the inferred retrograde displacements represent a predominantly inelastic deformation (e.g., frictional slip) on the pre-existing faults (5, 6, 9), they might be evidence that stress perturbations due to the mainshock may locally exceed the absolute (tectonic) stress resolved on the activated faults and, therefore, may be used to constrain the magnitude and the degree of heterogeneity of the pre-seismic stress field. Alternatively, the observed fault displacements might represent a predominantly elastic response of compliant fault zones to the co-seismic stress perturbations, dependent on the effective width of the fault zone and the rigidity contrast with the surrounding rocks but independent of the absolute background stress. Here we combine InSAR observations of strain localization on pre-existing faults in the Eastern California Shear Zone (ECSZ) due to the M_w 7.1 Hector Mine earthquake with models of the co-seismic stress change to investigate the in situ mechanical properties of active seismogenic faults.

The Hector Mine earthquake occurred on 16 October 1999, within the ECSZ (Fig. 1A). The earthquake area was repeatedly imaged by the European Space Agency satellites ERS-1 and ERS-2 over the past 10 years. We generated and analyzed all possible interferometric pairs that include the earthquake date, have a time span of less than 5 years, and have perpendicular baselines less than 200 m (10). This includes 14 independent (i.e., not sharing a common radar acquisition) interferograms from the descending orbit (satellite track 127) and 5 interferograms from the ascending orbit (track 77). Effects of topography were removed from the interferograms using a digital elevation model (DEM) produced by the Space Shuttle Radar Topography Mission (SRTM) (11). Analysis of multiple co-seismic interferograms allows us to select the interferometric pairs that are the least affected by the atmospheric noise (12) (Table 1).

To obtain a model-independent estimate of the character and magnitude of deformation induced by the Hector Mine earthquake on the neighboring faults, we removed the dominant co-seismic signal by high-pass filtering of the unwrapped interferograms. We used a two-dimensional box-car filter with a cut-off spatial wavelength of 7 km. High-pass filtered interferograms revealed that most of the faults adjacent to the Hector Mine rupture show localized line of sight (LOS) displacements of several millimeters to a few centimeters (Fig. 1B). The displacement lineaments are of tectonic origin and are not due to atmospheric effects or DEM errors because: (i) The displacement pattern (Fig. 1B) is present in all co-seismic interferograms (Fig. 2) but not in any pre- or post-seismic pairs. (ii) The displacement lineaments are correlated with the mapped faults. (iii) Un-

realistically large topographic errors of several hundred meters or greater would be required to produce the observed centimeter-scale changes in the radar range (13). (iv) The observed range

changes do not depend on the perpendicular baseline as one would expect if the anomalous lineations were due to DEM errors.

Of particular interest are variations in the

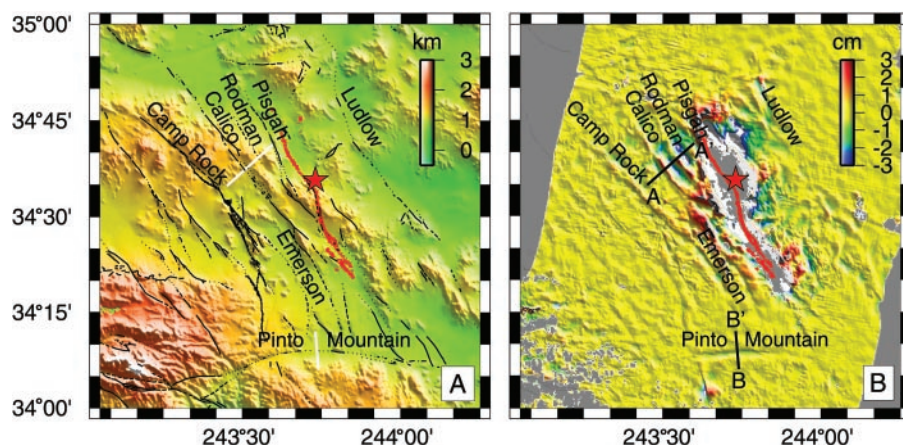


Fig. 1. (A) Shaded relief map of the epicentral area of the Hector Mine earthquake. The Hector Mine rupture is shown in red. Black curvy lines show the geologically mapped faults. Star denotes the epicenter of the Hector Mine earthquake (116.27°W , 34.595°N). (B) High-pass-filtered co-seismic interferogram from the descending orbit (IP 3). Colors and shading denote variations in the radar line of sight displacements. The lined anomalies ("troughs" and "ridges") in the LOS displacements are correlated with the pre-existing faults. LOS displacements toward the satellite (i.e., decreases in the radar range) are taken to be positive.

Table 1. The co-seismic interferometric pairs. Descending, d; ascending, a.

Pair	Acquisition dates	Orbit	B_{\perp} (m)
IP1	17 June 1998 to 29 December 1999	d	112
IP2	28 January 1998 to 24 November 1999	d	167
IP3	13 January 1999 to 20 October 1999	d	52
IP4	16 December 1995 to 26 December 1999	a	63
IP5	12 November 1995 to 21 November 1999	a	55
IP6	12 November 1995 to 1 October 2000	a	85

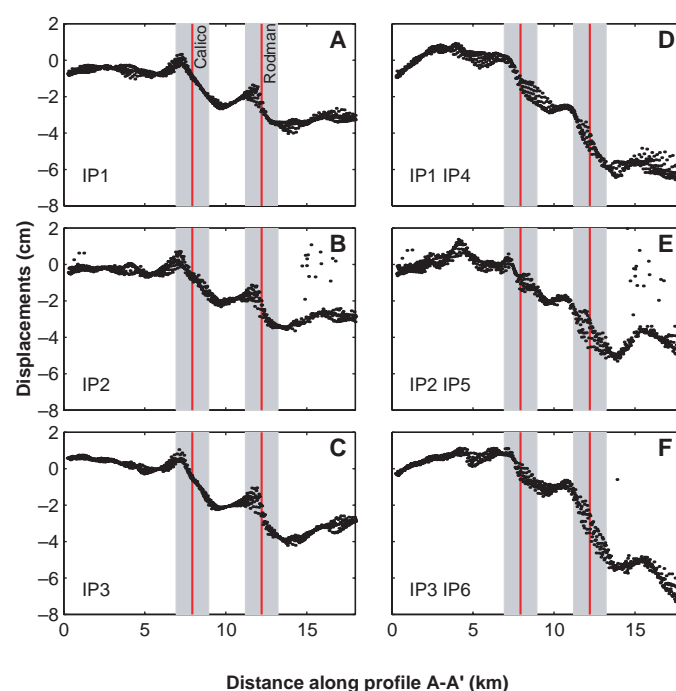


Fig. 2. Residual LOS displacements (data minus the best-fitting slip model for the Hector Mine earthquake) from the 2-km-wide swath along the profile AA'. (A to C) Residual LOS from the descending orbit. (D to F) Difference between the normalized residual LOS displacements from the descending and ascending orbits. Red lines denote the position of the geologically mapped faults, and gray shading denotes areas within 1 km from the mapped fault traces. The shaded areas approximately coincide with high gradients in the satellite LOS displacement (in particular, horizontal displacements [(D) to (F)]).

LOS displacements along the Calico and Rodman faults to the northwest of the epicenter of the Hector Mine earthquake (Fig. 1B). The InSAR data indicate an increase in the radar range as one traverses the faults from west to east. This result implies a left-lateral motion on the right-lateral Calico and Rodman faults, assuming that the deformation is pure strike-slip (6). The short-wavelength variations in the radar LOS displacements are unlikely to be due to some peculiar distribution of slip on the Hector Mine rupture, provided that the upper crust deforms as a transversely isotropic elastic medium. The residual LOS displacements [data minus the best-fitting slip model for the Hector Mine earthquake (12)] exhibit the same pattern as that deduced from the high-pass filtered data (Fig. 2, A to C). The anomalous “saw-tooth” LOS displacements around the pre-existing faults do not show any time dependence (in particular, their amplitude is constant in interferograms with different time spans), suggesting that they were induced co-seismically or shortly after (within 4 days) the earthquake.

We resolve the ambiguity between horizontal and vertical displacements associated with pre-existing faults by combining InSAR data from ascending and descending orbits. The difference between the normalized LOS displacements (14) from the two look directions

$$\Delta_{\text{los}} = \frac{d_{\text{los}}^{\text{d}}}{\cos\lambda^{\text{d}}} - \frac{d_{\text{los}}^{\text{a}}}{\cos\lambda^{\text{a}}} \quad (1)$$

is independent of the vertical component of the displacement field (15) (Fig. 2, D to F). In Eq. 1, d_{los} are the measured LOS displacements, λ is the radar incidence angle (on average, 23° from vertical), and superscripts a and d denote ascending and descending orbits, respectively. The Calico and Rodman faults of the ECSZ are associated with ~2-km-wide zones of high hor-

izontal strain (see shaded areas in Fig. 2, D to F). The observed gradients in horizontal displacements imply several centimeters of either fault-parallel (left-lateral) motion or fault-normal contraction, or some combination of both (16). Assuming no net vertical deformation away from the fault zones, the inferred horizontal displacements are predominantly fault-parallel if the across-fault variations in $d_{\text{los}}^{\text{d}}$ are comparable to variations in $\Delta_{\text{los}}^{\text{d}}$ and they are predominantly fault-normal if $|d_{\text{los}}^{\text{d}}| \ll |\Delta_{\text{los}}^{\text{d}}|$. Thus, the InSAR data (Fig. 2) likely represent both left-lateral motion and collapse within kilometer-wide shear zones centered on the pre-existing faults. Dissimilar patterns of $d_{\text{los}}^{\text{d}}$ and $\Delta_{\text{los}}^{\text{d}}$ (compare Fig. 2, A to C with D to F) suggest that the inferred shear zones are also associated with a local uplift. Calculations assuming either fault-parallel or fault-normal horizontal displacements indicate that the uplift amplitude is of the order of 1 cm.

We interpret these observations as indicating the presence of zones of reduced elastic moduli around the faults. Assuming linear elasticity, an order-of-magnitude estimate of the residual strike-slip displacement D across the fault zone is

$$D = w\Delta\sigma_t \left(\frac{1}{G'} - \frac{1}{G} \right) \quad (2)$$

where w is the width of a fault zone, $\Delta\sigma_t$ is the shear stress change, G' is the shear modulus of the fault zone, and G is the shear modulus of the ambient “intact” rocks. From Eq. 2, one may obtain an expression for the effective rigidity contrast between the fault zone and the ambient rocks

$$\frac{G'}{G} = \frac{1}{\frac{DG}{w\Delta\sigma_t} + 1} \quad (3)$$

In Eq. 3, $DG/w\Delta\sigma_t$ represents a ratio between

the excess strain accommodated by a fault zone, D/w , and the elastic strain due to the mainshock, $\Delta\sigma_t/G$. Note that the right-hand side of Eq. 3 is independent of the absolute value of the reference shear modulus G , as the shear stress change $\Delta\sigma_t$ calculated using the co-seismic slip model is a linear function of G .

The effective width of the fault zone, w , may be directly estimated from the residual InSAR data (Figs. 1B and 2). The upper bound on the shear displacement across the fault zone, D , can be calculated assuming that the fault-normal contraction is negligible. Our results for the Calico and Rodman faults indicate $w \sim 2$ km and $D < 4$ to 8 cm (Fig. 2, D to F) (16). We calculate static stress changes due to the Hector Mine earthquake using a three-dimensional boundary element code DIS3D (17, 18), a fault slip model that best explains the co-seismic surface displacement data (12) (Fig. 3). A comparison of Fig. 1B and Fig. 3 shows that sections of the Calico and Rodman faults that exhibit left-lateral displacements and collapse have experienced left-lateral shear stress changes and fault-normal compression of a few megapascals. Given the shear stress perturbation $\Delta\sigma_t = 1$ MPa for $G = 33$ GPa (Fig. 3A), from Eq. 3 we obtain $G'/G \geq 0.43$ to 0.60. Thus, the inferred retrograde motion on the Calico and Rodman faults requires a reduction in the effective shear modulus by about a factor of two within 2-km-wide fault zones surrounding the geologically mapped fault traces. An independent estimate of the rigidity contrast between the fault zones and the surrounding rocks can be obtained using observations of vertical deformation across the fault zones. The elastic inhomogeneity model predicts a Poissonian extrusion of a compliant fault zone in the presence of a fault-normal compression. The estimated amplitude of the corresponding uplift is given by

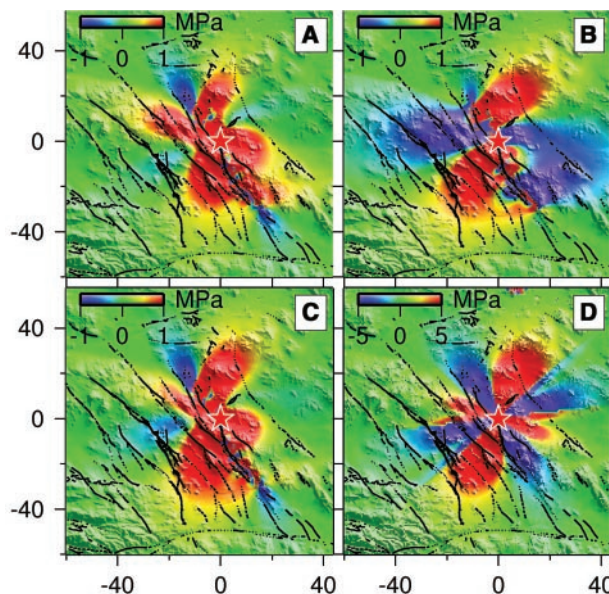
$$U = w\Delta\sigma_n \left(\frac{\nu'}{E'} - \frac{\nu}{E} \right) \quad (4)$$

where $\Delta\sigma_n$ is the perturbing normal stress resolved on the fault plane, E and ν are the Young modulus and the Poisson ratio of the host rocks, and primed variables denote the respective properties of rocks within the fault zone. For simplicity, we assume that variations in the Poisson ratio are small compared with variations in the shear modulus, $\nu \approx \nu'$. Making use of a known relation between the elastic parameters, $E = 2(1 + \nu)G$, Eq. 4 gives rise to an expression for the ratio of the shear modulus of the fault zone to that of the host rocks as follows

$$\frac{G'}{G} = \frac{1}{2 \frac{1 + \nu}{\nu} \frac{UG}{w\Delta\sigma_n} + 1} \quad (5)$$

For the inferred amplitude of the fault zone

Fig. 3. Static and dynamic stress changes due to the Hector Mine earthquake, in megapascals, on faults striking 35°NW, at depth of 2 km. (A) Static shear stress change. (B) Static normal stress change. (C) Static Coulomb stress change. (D) Maximum dynamic Coulomb stress change. The dynamic stress changes are computed using a point source model that fits seismic waveforms recorded by the continuous GPS stations of the SCIGN network (26). Extensional, and left-lateral shear and Coulomb stress changes are considered to be positive. Coulomb stress changes are computed assuming the coefficient of friction of 0.4. Horizontal coordinates are in km, with origin at the Hector Mine epicenter.



REPORTS

extrusion $U \sim 1$ cm, $w = 2$ km, and $\Delta\sigma_n = 2$ MPa (Fig. 3B) and assuming $\nu = 0.25$, we obtain $G'/G \sim 0.55$, similar to the predictions of Eq. 3. The elastic inhomogeneity model implies that the sign of the induced vertical deformation is controlled by the sign of the fault-normal stress (i.e., uplift for fault-normal compression and subsidence for fault-normal extension). An examination of Figs. 1B and 3B shows that such a correlation exists for the northwest-striking faults of the ECSZ. Furthermore, modeling of stress changes resolved on the east-west striking Pinto Mountain fault (Fig. 1) indicates that the latter has experienced a decrease in the fault-normal compression of about 0.6 MPa, whereas the change in the fault-parallel shear stress is negligible. The residual LOS displacement data from both the ascending and descending orbits indicate range increases (i.e., subsidence) of ~ 0.5 cm across a few-km-wide zone associated with the Pinto Mountain fault (see fig. S1).

We have verified order-of-magnitude estimates of deformation due to compliant fault zones using a finite element model of an elastic half-space containing a vertical layer of a softer material. The finite element simulations are performed using a commercial three-dimensional code ABAQUS. We calculate the surface displacements around the compliant layer due to uniform normal and shear stresses in the far field. The far-field boundary conditions are imposed using co-seismic stress perturbations on the modeled faults inferred from our kinematic model of the Hector Mine earthquake (e.g., Fig. 3). The modeled LOS displacements due to compliant zones around the Rodman and Pinto Mountain faults are shown in Fig. 4 and fig. S1, respectively. Our numerical experiments confirm the general predictions of Eqs. 3 and 5 and demonstrate that the elastic inhomogeneity model is consistent with the data. In addition, the finite element simulations allow us to examine the effects of possible two-dimensional variations in the effective elastic properties of the fault zones (e.g., variations in the fault zone rigidity with depth, as well as across-strike). Our calculations show that the InSAR data require significant (50 to 100%) reductions in the fault zone rigidity within a few kilometers from the surface. The maximum depth extent of the compliant fault zones cannot be readily estimated from the available data due to the essential three-dimensionality of the perturbing stress field (e.g., the assumption of a constant perturbing stress is not valid for a model that includes both Calico and Rodman faults) and due to a decreasing signal-to-noise ratio in the far field (i.e., beyond several kilometers from the faults). Our numerical experiments suggest that the deformation pattern around the Calico and Rodman faults may be indicative of

the compliant fault zones that are a few kilometers deep (Fig. 4). The rigidity reductions associated with the Pinto Mountain fault may extend to greater depths (fig. S1).

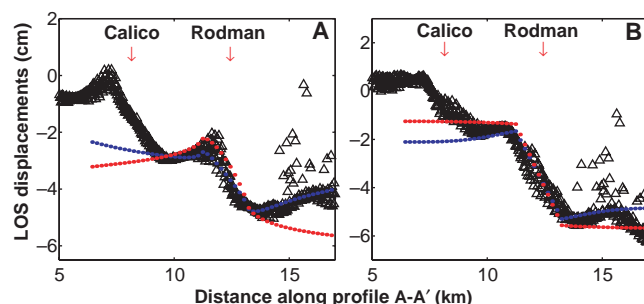
We also consider a possibility that the observed strain localization along the pre-existing faults might result from the induced slip (i.e., frictional yielding) due to the co-seismic static or dynamic stress changes (5, 6). We estimate the magnitude and distribution of the hypothesized slip on the Calico and Rodman faults by inverting the residual LOS data from both orbits. The faults are approximated by arrays of dislocations in either homogeneous or horizontally layered elastic half-space. Our calculations indicate that although the data from the descending orbit alone may be satisfactorily explained by a pure left-lateral slip on the Calico and Rodman faults, the joint inversion of the ascending and descending data requires more than one mode of deformation. Figure S2 shows the stacked residual LOS data from the profile AA' along with predictions of the best-fitting models of displacement on the Calico and Rodman faults for the homogeneous elastic half-space. A combination of strike-slip and dip-slip displacements only slightly decreases the model misfit, whereas a combination of strike-slip and fault-normal displacements is able to explain most of the observed signal. The depth distribution of the induced strike-slip and fault-normal displacements on the Calico and Rodman faults obtained from our inversion is shown (fig. S2, C and D). We infer up to ~ 10 to 20 cm of left-lateral slip and fault-normal contraction in the depth interval between 1 and 3 km. Accounting for possible increases in the shear modulus of the upper crustal rocks with depth gives rise to somewhat greater depths of the inferred slip. The induced slip is not well-resolved below ~ 3 km, because the residual range changes at distances greater than several kilometers away from the faults are dominated by the atmospheric noise and the misfit between the data and the mainshock model.

Because both the dynamic and static Coulomb stress changes are small compared with

the lithostatic stress within the inferred slip depths of 1 to 3 km (19) (Fig. 3), the frictional yielding model implies that the pre-seismic stress resolved on the upper few kilometers of the back-slipped faults was considerably less than that predicted by the strong fault theory assuming Byerlee's law and the hydrostatic pore pressures (20). In addition, the in situ coefficient of fault friction must be considerably less than the laboratory-derived values of 0.6 to 0.8 (21), provided that the pre-seismic stress is not left-lateral. However, there exist several contravening arguments that question the applicability of the frictional yielding model: (i) It is not clear why the induced left-lateral slip did not reach the surface, given that the fault strength increases with depth, whereas the co-seismic stress change is nearly constant. (ii) No retrograde slip is observed to the southwest of the epicentral area where the models predict the largest left-lateral Coulomb stress changes (Fig. 3). (iii) A physical mechanism for the inferred fault collapse is not obvious. (iv) The observed subsidence along the Pinto Mountain fault cannot be easily explained in terms of the frictional slip model. Therefore, we conclude that the elastic inhomogeneity model better explains the observations.

The kilometer-wide zones of reduced rigidity imaged with InSAR may represent the mechanically weakened damage zones around the faults. The existence of such zones has been suggested based on field studies of the exhumed fault zones (20) and observations of low-velocity seismic wave guides along several major strike-slip faults (22–24). For example, the fault wave guide studies of the 1992 Landers earthquake that occurred 20 km to the west from the Hector Mine event (22, 25) revealed a low-velocity zone below the surface rupture of the earthquake with shear wave velocity reductions of the order of 40 to 50%. Assuming no variations in the rock density, the observed seismic velocity reductions imply a decrease in the shear modulus of a factor of two or more, similar to the results of our study. The inferred width of the Landers wave guide is ~ 200 m (22, 25). Although this is less than our estimate

Fig. 4. Finite element modeling of deformation due to a compliant fault zone around the Rodman fault. The data (black triangles) represent (A) average LOS displacements from the descending orbit d_{los}^d , and (B) average differential LOS displacements Δ_{los} (Table 1, Fig. 2). Color dots show the model predictions for a 2-km-wide compliant fault zone that is (i) unlimited with depth (red dots) and (ii) restricted to the uppermost 2 km (blue dots). The fault-normal stress is taken to be 3 MPa, and shear stress is 2 MPa (Fig. 3). The inferred best-fitting ratio between the shear moduli of the fault zone rocks and the host rocks is $G'/G = 0.67$.



of ~2 km for the Calico, Rodman, and Pinto Mountain faults, variations in the radar LOS displacements across the southern part of the Landers rupture are indicative of a rather narrow (several hundred meter wide) deformation zone (Fig. 1), apparently in agreement with the seismic studies. These observations suggest that the mechanical properties of seismogenic fault zones (the fault zone width, and the rigidity contrast with the surrounding rocks) may vary considerably, perhaps manifesting a cumulative damage from past earthquakes, and time-dependent healing in the interseismic period. If so, probing of the mechanical structure of seismogenic faults may help to identify various stages of the earthquake cycle for individual faults.

References and Notes

1. R. Sharp, M. Rymmer, J. Lienkaemper, *Bull. Seismol. Soc. Am.* **76**, 949 (1986).
2. C. M. Poley, A. G. Lindh, W. H. Bakun, S. S. Schulz, *Nature* **327**, 134 (1987).
3. R. Harris, R. Simpson, P. Reasenber, *Nature* **375**, 221 (1995).
4. E. Price, D. T. Sandwell, *J. Geophys. Res.* **103**, 27001 (1998).
5. T. Wright, E. Fielding, B. Parsons, *Geophys. Res. Lett.* **28**, 1079 (2001).
6. D. Sandwell, L. Sichoix, D. Agnew, Y. Bock, J.-B. Minster, *Geophys. Res. Lett.* **27**, 3101 (2000).
7. Y. Fialko, M. Simons, D. Agnew, *Geophys. Res. Lett.* **28**, 3063 (2001).
8. Previous inferences about the retrograde fault motion due to nearby earthquakes are uncertain because the interferometric data from only one look direction do not allow one to distinguish between the horizontal and vertical components of deformation.
9. If the retrograde fault displacement is due to frictional slip, the latter is more appropriately referred to as induced rather than triggered, because the causative stress change may not be small compared with the pre-existing stress.
10. Perpendicular baseline is a distance between the master and repeat satellite orbits in direction orthogonal to the radar line of sight. Small perpendicular baselines diminish sensitivity of the interferometric data to topography and reduce radar lay-overs in areas of steep topography.
11. T. G. Farr, M. Kobrick, *Eos* **81**, 583 (2000).
12. M. Simons, Y. Fialko, L. Rivera, *Bull. Seismol. Soc. Am.* **92**, 1390 (2002).
13. The nominal errors in the SRTM data are of the order of a few meters.
14. We normalize LOS displacements d_{los} by the cosine of the radar incidence angle to account for small but non-negligible variations in the incidence angle across the radar image.
15. P. Rosen *et al.*, *Proc. IEEE* **88**, 333 (2000).
16. For the orbital parameters of the ERS satellites, the along-fault displacement $U_{||} \approx -1.21\Delta_{los}/\cos(\theta-1.56)$, where θ is the fault strike in radians, provided that the fault-perpendicular displacement, U_{\perp} , is zero. A positive $U_{||}$ displacement is left-lateral if θ is taken to be positive counterclockwise from North. For the Calico and Rodman faults striking ~35°NW, $U_{||} \approx -2.1\Delta_{los}$. For the same fault geometry and assuming $U_{\perp} = 0$, $U_{\perp} \approx -1.5\Delta_{los}$.
17. A. M. Rubin, *J. Geophys. Res.* **97**, 1839 (1992).
18. Y. A. Fialko, A. M. Rubin, *J. Geophys. Res.* **104**, 20,007 (1999).
19. The co-seismic stress changes shown in Fig. 3 are upper bounds because the shear modulus of the uppermost crust is likely less than the assumed value of 33 GPa. The lithostatic stress σ_l equals the weight of the overburden, $\sigma_l = \rho g z$, where ρ is the rock density, g is the gravitational acceleration, and z is depth. For $z = 1$ to 3 km, σ_l is of the order of tens of megapascals.
20. C. H. Scholz, *The Mechanics of Earthquakes and Faulting* (Cambridge Univ. Press, New York, 1990).

21. J. Byerlee, *Pure Appl. Geophys.* **116**, 615 (1978).
22. Y. Li, J. Vidale, K. Aki, C. Marone, W. Lee, *Science* **265**, 367 (1994).
23. Y. Li, W. Ellsworth, C. Thurber, P. Malin, K. Aki, *Bull. Seismol. Soc. Am.* **87**, 210 (1997).
24. Y. Ben-Zion, *J. Geophys. Res.* **103**, 12567 (1998).
25. Y. Li, J. Vidale, K. Aki, F. Xu, T. Burdette, *Science* **279**, 217 (1998).
26. R. Nikolaidis *et al.*, *J. Geophys. Res.* **106**, 21897 (2001).
27. We thank J. Vidale, P. Segall, and anonymous reviewers for their thoughtful comments. This work was supported by the Southern California Earthquake

Center and NSF. Original InSAR data are copyright of the European Space Agency, distributed by Eurimage, Italy, and acquired via the WInSAR Consortium. The ERS SAR imagery was processed using the Caltech/JPL software package ROI_PAC.

Supporting Online Material

www.sciencemag.org/cgi/content/full/297/5588/1858/DC1

Figs. S1 and S2

4 June 2002; accepted 12 August 2002

Relative Timing of Deglacial Climate Events in Antarctica and Greenland

Vin Morgan,^{1*} Marc Delmotte,^{2,3*†} Tas van Ommen,^{1,‡} Jean Jouzel,³ Jérôme Chappellaz,² Suenor Woon,¹ Valérie Masson-Delmotte,³ Dominique Raynaud²

The last deglaciation was marked by large, hemispheric, millennial-scale climate variations: the Bølling-Allerød and Younger Dryas periods in the north, and the Antarctic Cold Reversal in the south. A chronology from the high-accumulation Law Dome East Antarctic ice core constrains the relative timing of these two events and provides strong evidence that the cooling at the start of the Antarctic Cold Reversal did not follow the abrupt warming during the northern Bølling transition around 14,500 years ago. This result suggests that southern changes are not a direct response to abrupt changes in North Atlantic thermohaline circulation, as is assumed in the conventional picture of a hemispheric temperature seesaw.

The last glacial period and glacial-interglacial transition were marked by large, millennial-scale climate changes that followed a general north-south pattern, the relative timings of which have been examined for indications of forcing and coupling mechanisms (1–10). The geographical scale and abruptness of these changes and their apparent absence in the Holocene point to nonlinearities in global climate dynamics and a sensitivity of climate stability to the mean state of the system (6, 11). The stability of a future climate with a mean state forced beyond natural interglacial-Holocene variability is an important issue that is

addressable with climate models, but these models first need to be able to reproduce the past behavior before their predictions can be considered robust. Model simulations now can capture some important features of the observed glacial climate changes (6), and insights have been gained into the patterns and pacing relationships exhibited in the paleorecords (12), but verification depends critically on the ability to synchronize paleorecords and thereby establish the relative timing of millennial-scale changes across the globe.

The observed pattern for the millennial changes in the last glacial period can be summarized as follows. The cold (stadial) phase is interrupted by an abrupt northern warming event (interstadial), then gradual cooling occurs at a rate that may be related to total ice volume (12), before a return to glacial conditions. The final return to glacial conditions is frequently marked by a rapid cooling, which is smaller than the initial warming jump. These events, commonly known as Dansgaard-Oeschger (DO) events, are sometimes accompanied by a second series of cooling events, called Heinrich (H) events. H events occur during stadial periods and show little additional cooling signal in Greenland, but are thought to involve much larger changes in thermohaline circulation (7). The Antarctic expression of these events is quite

¹Antarctic Cooperative Research Centre and Australian Antarctic Division, GPO Box 252-80, Hobart, Tasmania, Australia. ²CNRS/Laboratoire de Glaciologie et Géophysique de l'Environnement, 54 Rue Molière, B.P. 96, 38402 St. Martin d'Hères Cedex, France. ³Institut Pierre-Simon Laplace Laboratoire des Sciences du Climat et l'Environnement, Unite Mixte de Recherche Commissariat à l'Energie Atomique-CNRS 1572, l'Orme des Merisiers, CEA Saclay, 91191 Gif sur Yvette Cedex, France.

*These authors contributed equally to this work.
 †Present address: CNRS/Institut de Physique du Globe de Paris, Laboratoire de Cosmochimie et Géochimie, 4 place Jussieu tour 14, 3ème étage, 75252 Paris Cedex 05, France.
 ‡To whom correspondence should be addressed. E-mail: tas.van.ommen@utas.edu.au